Integrating LEO and GEO Observations: Toward Optimal Summertime Satellite Precipitation Retrieval

VESTA AFZALI GOROOH,[a] VELJKO PETKOVIĆ,[b] MALARVIZHI ARULRAJ,[b] PHU NGUYEN,[a] KUO-LIN HSU,[a] SOROOSH SOROOSHIAN,[a,c] AND RALPH R. FERRARO[b]

[a] *Center for Hydrometeorology and Remote Sensing, Department of Civil and Environmental Engineering, University of California, Irvine, Irvine, California*
[b] *Cooperative Institute for Satellite Earth System Studies, Earth System Science Interdisciplinary Center, University of Maryland, College Park, College Park, Maryland*
[c] *Department of Earth System Science, University of California, Irvine, Irvine, California*

ABSTRACT: Reliable quantitative precipitation estimation with a rich spatiotemporal resolution is vital for understanding the Earth's hydrological cycle. Precipitation estimation over land and coastal regions is necessary for addressing the high degree of spatial heterogeneity of water availability and demand, and for resolving the extremes that modulate and amplify hazards such as flooding and landslides. Advancements in computation power along with unique high spatiotemporal and spectral resolution data streams from passive meteorological sensors aboard geosynchronous Earth-orbiting (GEO) and low Earth-orbiting (LEO) satellites offer exciting opportunities to retrieve information about surface precipitation phenomena using data-driven machine learning techniques. In this study, the capabilities of U-Net–like architecture are investigated to map instantaneous, summertime surface precipitation intensity at the spatial resolution of 2 km. The calibrated brightness temperature products from the Global Precipitation Measurement (GPM) Microwave Imager (GMI) radiometer are combined with multispectral images (visible, near-infrared, and infrared bands) from the Advanced Baseline Imager (ABI) aboard the GOES-R satellites as main inputs to the U-Net–like precipitation algorithm. Total precipitable water and 2-m temperature from the Global Forecast System (GFS) model are also used as auxiliary inputs to the model. The results show that the U-Net–like algorithm can capture fine-scale patterns and intensity of surface precipitation at high spatial resolution over stratiform and convective precipitation regimes. The evaluations reveal the potential of extracting relevant, high spatial features over complex surface types such as mountainous regions and coastlines. The algorithm allows users to interpret the inputs' importance and can serve as a starting point for further exploration of precipitation systems within the field of hydrometeorology.

KEYWORDS: Precipitation; Remote sensing; Satellite observations; Neural networks; Deep learning

1. Introduction

Conventional in situ gauges and weather radars are the most reliable resources for measuring surface precipitation. However, the uneven distribution of the ground-based instruments is insufficient to fully capture temporal and spatial variability of the precipitation phenomena. In recent decades, extending observational capabilities through meteorological satellites has provided sustained information that promotes high-spatiotemporal-resolution precipitation retrievals on a global scale and addresses the shortcomings of conventional precipitation measurements (Skofronick-Jackson et al. 2017; Kidd and Levizzani 2011). Satellite precipitation estimation algorithms offer pivotal data for water resource management, natural hazard monitoring, and forecasts. However, intercomparison of high-spatiotemporal-resolution surface precipitation products has shown significant discrepancies and limitations in different regions (You et al. 2020; Saemian et al. 2021; Beck et al. 2019; Gorooh

et al. 2022b; Mallakpour et al. 2022). Precipitation is a consequence of highly dynamical processes and, therefore, frequent observations are essential for capturing the evolving features of its environment. The current constellation of satellite passive microwave (PMW) radiometers on low-Earth-orbit (LEO) platforms is insufficient for monitoring the evolution of rapid precipitation events. Due to the coarse spatial resolution of PMW observations, their associated retrievals have limited skills in capturing fine spatial patterns of surface precipitation rates over nonhomogeneous surface types (Utsumi et al. 2021; You et al. 2020). Still, PMW retrievals are the backbone of global precipitation monitoring and have successfully delivered rainfall estimates since the early 1980s. One example is the state-of-the-art NASA's Goddard profiling (GPROF) algorithm (Kummerow et al. 2015) serving various PMW sensors in the Global Precipitation Measurement (GPM) mission, delivering consistent estimates of vertical profiles and surface precipitation.

Another category of meteorological passive sensors is aboard geostationary satellite (GEO). These sensors are mainly sensitive to the visible (VIS) and infrared (IR) parts of the electromagnetic spectrum, offer quasi-global coverage in high spatiotemporal resolution with a latency lower than 15 min. Although the products from GEO sensors mostly rely on cloud-top properties, their virtually continuous monitoring makes them suitable for near-

real-time and high-spatial-resolution precipitation estimation purposes. The Self-Calibrating Multivariate Precipitation Retrieval (SCaMPR; Kuligowski et al. 2016), the Precipitation Estimation from Remotely Sensed Information Using Artificial Neural Networks (PERSIANN; Hsu et al. 1997; Hong et al. 2004; Nguyen et al. 2020a; Sorooshian et al. 2000), and the Hydro-Estimator (HE; Scofield and Kuligowski 2003) are widely used, operational, GEO-based precipitation retrieval algorithms that employ a limited range of IR measurements as their primary inputs. In recent years, the advanced generation of GEO passive sensors, such as the Advanced Baseline Imager (ABI) on the GOES-R satellite series, the Advanced Himawari Imager (AHI) on *Himawari-8/9*, and the Advanced Meteorological Imager (AMI) aboard *GEO-KOMPSAT-2A* satellites, has introduced measurement of the reflected and emitted radiances of a higher number of spectral bands. These sensors provide multispectral information at a spatial resolution of 0.5–2 km with 5–15-min temporal sampling (Schmit et al. 2017). Although high spatiotemporal data streams from the latest GEO sensors are highly attractive, their complete spectral information is underutilized in precipitation applications (Upadhyaya et al. 2022b).

Over the past 40 years, the development of precipitation algorithms using different satellite remotely sensed information has been an ongoing effort (Adler et al. 1993; Arkin and Ardanuy 1989; Hsu et al. 1997; Joyce et al. 2004; Aonashi et al. 2009; Foufoula-Georgiou et al. 2020; Hong et al. 2004; Nguyen et al. 2020b; Ferraro 1997; Kummerow et al. 2015). Recent fast-growing advancements in satellite remote sensing technologies, along with the unprecedented growth of promising machine learning applications (especially in Earth system sciences), offer attractive opportunities for improving the accuracy of precipitation products. Examples include, but are not limited to, the use of random forest (RF; Ouallouche et al. 2018; Upadhyaya et al. 2022b) and neural networks (NNs; Akbari Asanjan et al. 2018; Sadeghi et al. 2020; Meyer et al. 2017; Upadhyaya et al. 2022a; Pfreundschuh et al. 2022). Behrangi et al. (2009) demonstrate the improvements in delineating rain/no-rain areas obtained by adding VIS channels in conjunction with near-infrared (NIR) channels from the *GOES-13* imager to an NN-based model. Hirose et al. (2019) and Min et al. (2019) present RF-based algorithms that use NIR and IR brightness temperatures (Tbs) from AHI for precipitation quantification. Hayatbini et al. (2019) use a combination of ABI information to develop an advanced NN-based surface precipitation retrieval algorithm. For PMW precipitation algorithms, similar improvements are documented. Passive Microwave Neural Network Precipitation Retrieval (PNPR) by Sanò et al. (2016) and the work by Li et al. (2021) are among the more recent NN-based, PMW-retrieving precipitation algorithms. Research on the operational GPROF algorithm presents an outstanding potential for modern NN approaches to improve the accuracy and effective resolution of retrieved surface precipitation rates and hydrometeor profiles from GPM PMW observations (Pfreundschuh et al. 2022). Recently, Gorooh et al. (2022a) introduced a deep neural network (DNN) framework that fuses a single IR channel (~10 μm) from GEO platforms with LEO PMW measurements to retrieve high-spatiotemporal-resolution surface precipitation. According to the results from their Deep Neural Network High

Spatiotemporal Resolution Precipitation (Deep-STEP) Model, there is a promising opportunity for capturing fine-scale precipitation patterns over complex surface types. Their algorithm can achieve similar or better surface precipitation estimates than the operational NASA Integrated Multi-satellitE Retrievals for the GPM mission (IMERG) V06 early run and Microwave Imager (GMI) GPROF V05 algorithms during both warm and cold seasons of year. However, Deep-STEP faces challenges in surface precipitation detection during warm months.

Upon literature review, motivated by the shortcomings of the studies listed above, it has been noted that no documented study attempts to utilize complete and direct information content provided by all available passive satellite sensors covering VIS, NIR, and IR parts of the electromagnetic spectrum as well as the emission and scattering frequencies from passive microwave bands to derive high-resolution surface precipitation rates. This study aims to develop a DNN framework that fuses the existing passively sensed information from GEO and LEO satellites with respect to the spatiotemporal properties of summertime precipitation systems with a goal to test this unexplored opportunity. Specifically, we aim to address two questions: 1) What are the potentials of implementing DNNs that use ultimate information from LEO PMW radiometers, multispectral observations from GEO satellites, and ancillary variables from numerical weather prediction models to improve surface precipitation retrievals during summertime? And 2) Can a simple end-to-end DNN model integrating multiple sources of information in near-real time offer a comparable performance to that of the current state-of-the-art precipitation algorithms? To seek answers to these questions, the study targets the development of a U-Net–like precipitation algorithm for a wide range of VIS, NIR, and IR images from ABI sensors (0.47–13 μm) combined with PMW Tbs from the GMI radiometer (10–183 GHz), along with the ancillary variables (2-m temperature and total column atmosphere precipitable water) from the Global Forecast System (GFS). Then, the retrieved precipitation rates from our model are evaluated over various surface types and over stratiform and convective regimes. The capabilities of our DNN model are presented along with the performance of operational, global-scaled satellite precipitation algorithms to assess how close we can get to these highly specialized and widely used precipitation retrievals. Following the introduction, this paper is organized as follows: Section 2 presents the data sources and study area. Section 3 introduces a U-Net–like architecture and explains the methodology, followed by the results and discussion in section 4. Finally, section 5 summarizes the investigation and provides concluding remarks.

2. Data and study region

A variety of datasets with different spatial and temporal resolutions, including passive remotely sensed information from GEO and LEO satellites, active sensors on LEO satellites, numerical weather prediction models, and precipitation products from satellite and ground-based platforms, are used in the investigations documented here. Given the availability of high-quality reference data, as indicated by the quality indices, the study considers the months June–September in a 4-yr

period (2017–20) over the eastern contiguous United States (CONUS) and parts of the North Atlantic Ocean near a coastal region (105°–60°W and 20°–45°N).

a. ABI data

ABI is a unique 16-band radiometer with spectral bands covering the electromagnetic spectrum at VIS, NIR, and IR frequencies. The ABI aboard the *GOES-16* satellite scans the CONUS every 5 min in two VIS bands: 0.47 and 0.64 μm, with approximate 1- and 0.5-km spatial resolution, respectively. The emitted radiances from four NIR bands—0.86, 1.37, 1.6, and 2.2 μm—and 10 IR bands—3.9, 6.2, 6.9, 7.3, 8.4, 9.6, 10.3, 11.2, 12.3, and 13.3 μm—are measured with approximate 2-km spatial resolution, except for the 1-km resolution channels at 0.86 and 1.61 μm (Schmit et al. 2017). This study uses the high spatial and temporal resolution NOAA Level-2 Cloud and Moisture Imagery product (CMIP) from the *GOES-16* ABI to obtain the radiances and Tbs at all 16 bands.

b. Solar altitude angle

In this study, solar altitude angle is used to address the effects of the sun's position on GEO-based measured radiances. ABI observes Earth at a fixed-view angle. Yet, the solar angle at a given pixel is a function of the latitude and local time. With the assumption that *GOES-16* ABI is located at a fixed point above Earth, the instantaneous solar altitude angle is calculated for each ABI pixel (Wang et al. 2020; Ma et al. 2020; Kalogirou 2022).

c. GMI measurements

The GMI aboard the GPM *Core Observatory* (GPM-*CO*) satellite is a conical scanning radiometer that provides Tbs in two different scanning geometries. Swath S1 has a width of approximately 931 km and covers the microwave frequencies at nine channels and both vertical (V) and horizontal (H) polarizations: 10.65V/H, 18.7V/H, 23.8V, 26.6V/H, and 89V/H GHz. Swath S2 has a width of approximately 825 km, providing measurements at frequencies of 166V/H, 183.3 ± 3V, and 183.3 ± 7V GHz. Resampled Tbs, delivered by the GMI L1CR (version 07) product, in both emission and scattering frequencies, are used in the present study. The spatial resolution of GMI's field of view (FOV) varies from 32.1 km × 19.4 km for the 10V GHz channel to 5.6 km × 3.8 km for the 183.3 ± 3V GHz channel (Hou et al. 2014; Draper et al. 2015; Skofronick-Jackson et al. 2017).

d. GFS variables

In addition to GMI and ABI observations, 2-m temperature (T2m) and total column precipitable water (PWAT) variables from the National Centers for Environmental Prediction (NCEP) GFS model are used as ancillary inputs to the neural network framework. GFS output is available at 3-hourly time-step increments for the forecast products. The study combines GFS variables with high-spatiotemporal-resolution surface precipitation using GFS analysis at 0000, 0600, 1200, and 1800 UTC and forecast fields at 0300, 0900, 1500, and 2100 UTC at 0.25° spatial resolution.

e. Multi-radar multi-sensor

NASA Global Hydrology Resource Center provides the state-of-the-art GPM Ground Validation Multi-Radar Multi-Sensor (GV-MRMS) reanalysis at 1-km spatial resolution. This product combines Weather Surveillance Radar-1988 Doppler (WSR-88D) data with rain gauges, satellite, and environmental variables to deliver highly accurate quantitative precipitation estimates over the CONUS and parts of Canada (Kirstetter et al. 2012; Zhang et al. 2016). We used 2-min MRMS surface precipitation rates and a radar quality index (RQI) to establish a benchmark surface precipitation rate in this study.

f. Passive and active microwave precipitation products

PMW-based surface precipitation estimates from the operational, Bayesian-based GPROF version 07 retrieval (Kummerow et al. 2015), provided by the GPM Precipitation Processing System (2AGPROFGMI), and the recent NN-based GPROF (GPROF-NN 3D; Pfreundschuh et al. 2022), are used as a benchmark throughout the present study. Moreover, surface precipitation rates from GPM Dual-Frequency Precipitation Radar (DPR) product (2AGPMDPR, version 7) are presented in the investigation to highlight the differences between active- and passive-based rain-rate products.

3. Methodology

a. U-Net–like architecture

A fully convolutional model with U-Net architecture is introduced by Ronneberger et al. (2015) for biomedical image segmentation. In this study, we use similar architecture on satellite passively sensed information to retrieve surface precipitation. Here, the supervised learning problem can be stated as $d: I \rightarrow O$, where domain I represents the input space—including VIS, NIR, IR, and PMW observations as well as GFS variables—and codomain O represents the output space (precipitation rate). The true d operator can be approximated by finding $Y = f(X; \Theta)$, where $Y \in O$ and $X \in I$. The $f()$ model is trained using N labeled training dataset $\{X^i, Y^i\}$, $i = 1, \ldots, N$ and Θ is the trainable parameter of model $f()$.

Figure 1 displays a schematic for the U-Net–like architecture, which consists of encoder, bottleneck, and decoder parts. The arrangement of the elements of each component is important for accomplishing sustained high performance while the model automatically learns complex features from the input datasets. In our U-Net–like model (hereafter, U-Net), the encoder blocks consist of a set of 2D kernels (kernel size = 5 × 5) with the same padding option, batch normalization, elementwise leaky rectified linear unit (ReLU) activation function, and maxpooling2D (pool size = 2 × 2) layers. These blocks downsample the input information to extract the detailed feature maps from their inputs. Kernels convolve over input layers and tune the learnable parameters by calculating loss function gradients with respect to each kernel weight. The maxpooling layer subsamples the maximum value of a sampling window to learn translation invariant features while reducing the encoder's computational complexity. The leaky ReLU function alleviates the "dying ReLU" problem. In the training of deep convolutional NNs
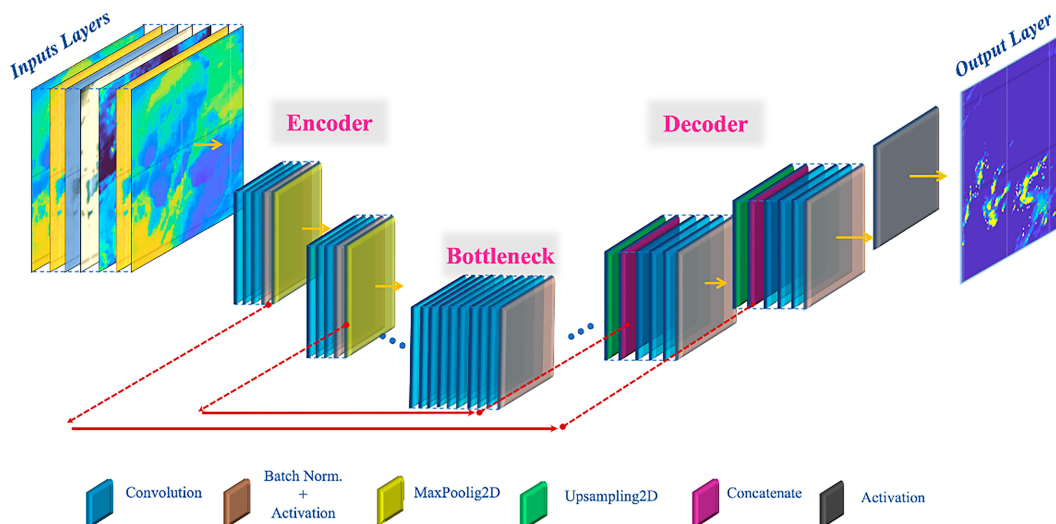
FIG. 1. U-Net–like architecture schematic. The encoder extracts robust features from input images, the decoder constructs the output patterns and pixel values, and the bottleneck is the connection between the encoder and decoder parts of the model.

(CNNs), an ReLU-based neuron can be trapped in negative values (especially in significant negative biases) and yield zero values. In such a scenario, these types of neurons do not perform well (discriminating the input), leading to the inefficiency of a large part of the CNN. The leaky ReLU function is defined as

$$f(\o) = \max\{0.01\o, \o\} \qquad (1)$$

In this case, the function f returns positive input ($\o$), whereas it returns a small value (0.01$\o$) for negative input. Thus, this function prevents the CNN model's deactivated regions (dead regions). After the encoder, the bottleneck receives highly condensed (low-dimensional) information from the input images. The decoder includes upsampling2D (upsampling size = 2 × 2), concatenate, batch normalization, and activation function (leaky ReLU) layers to expand the feature maps. The concatenate (skip connection) layer is a unique property of the U-Net algorithm that connects the preserved structural features from learned latent encoding to the decoding parts. This layer concatenates two same-level feature blocks (encoding features with decoding features) in the model and alleviates the vanishing gradient challenge in NN algorithms (Ehsani et al. 2021).

After the decoder, one convolutional layer with an ReLU activation function is typically used to retrieve the precipitation rates with the same size as the input. The 2D convolutional layer can be defined by

$$Y[i, j] = \sum_n \sum_m K[m, n] \, X[i - m, \, j - n], \qquad (2)$$

where Y is the result of the convolution of kernel K over input X, and m and n are dummy variables of the integration. The same padding option in the convolutional layers appends zero

values in the outer part of the input layers in order to conserve the size of the convolution layer output identical to the input layer. Figure 2 illustrates the convolution of an arbitrary 2 × 2 kernel across a 4 × 4 input with the same padding option. In fully convolutional algorithms, once the kernels and learnable parameters are defined (i.e., the model is trained), the model can operate and produce the appropriate dimension output according to the corresponding input (here, image-to-image conversion). "Equivariance to translation," "sparse connectivity," and "parameter sharing" properties of fully CNNs models (Goodfellow et al. 2016) enable the trained kernels to capture local and meaningful features when processing an input image, irrespective of their size.

b. Data sampling and integration

This study combines various types of information of different spatial and temporal resolutions originating from passive GEO and LEO satellite sensors, as well as the GFS model. Following the data integration strategy of Gorooh et al. (2022a), the nearest neighbor approach (Rukundo and Cao 2012) is employed to resample the swath datasets into a fixed 2-km grid. While potential errors from different interpolation strategies in the resampling procedure may occur, we estimate their impacts on the results presented here are insignificant. Figure 3 illustrates a schematic for the data preprocessing framework. Based on LEO orbital tracks (GMI PMW FOVs), the coordinated universal time (UTC) associated with the scan time is used to extract the closest 5-min GEO readings (VIS, NIR, and IR images from ABI), 3-hourly ancillary data from the GFS model (PWAT and T2m) and 2-min MRMS retrievals in their original spatial resolutions are selected. The spatial intersections of each of the datasets with the LEO orbital swaths are collocated and resampled into the 2-km grids. The nearest-neighbor approach is used for swath-to-grid conversions, with the bilinear interpolation approach for grid-to-grid resampling tasks.
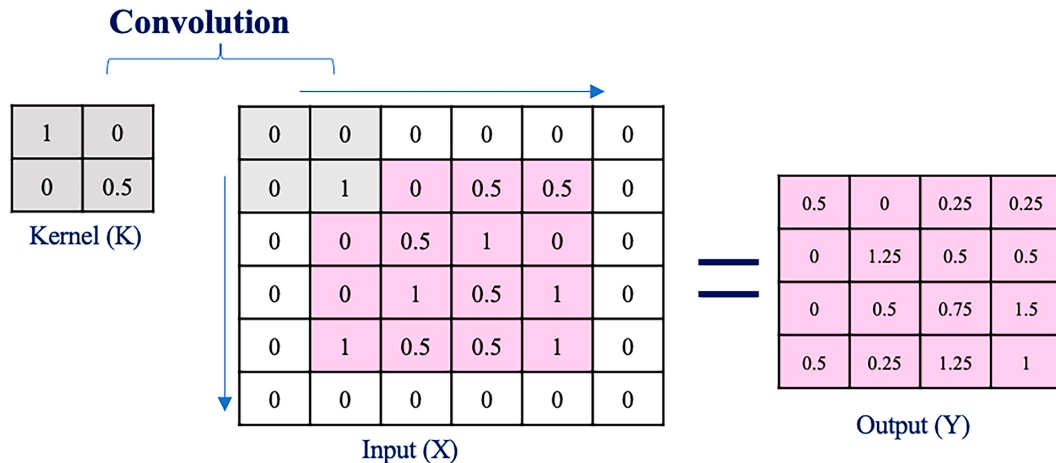
FIG. 2. A schematic for the convolution of a 2D kernel (K) over a 2D input data (X) with the same padding option; Y is the response to this convolution example.

With a goal to allow for the largest possible input features, given GMI swath width, the availability of spatially uniform high-quality reference products, the size of the model (trainable parameters), and the required computational power, the training dataset is generated using 128 km × 128 km patched samples. The collocated GMI Tbs, ABI reflectance and Tbs, GFS variables (PWAT, T2m), and MRMS surface precipitation rates for the areas with RQI values greater than 0.8 are organized into 64 × 64 pixel samples. These data patches are normalized and partitioned into the training, validation, and test subsets corresponding to nonoverlapping time periods. We used 80% and 20% of samples from May to September 2017–19 for training and validation purposes, respectively, while June–September of 2020 is considered an independent test period. No efforts are made to produce a balanced dataset.

A fully CNN with U-Net architecture is tasked to retrieve surface precipitation rates at 2-km spatial resolution. Based on sensitivity analyses and the availability of data (e.g., number of missing values, low quality index), GMI channels 2, 3, and 13, as well as ABI channels 5, 12, 15, and 16 are excluded from the list of the input features. Moreover, it has been found that using surface-type ancillary information [e.g., monthly emissivity climatology, Tool to Estimate Land Surface Emissivities at Microwave Frequencies (TELSEM); Prigent et al. 2003; Aires et al. 2011] in addition to low frequencies has an insignificant impact on the model's overall performance, while the number of learnable parameters and memory utilization during the training was increased. Their effects on the training process and accuracy of the retrieved surface precipitation estimates are insignificant. After the data sampling and integration, the dataset counts approximately 110 000 available samples (patches) for model training and validation. The information from the GMI and ABI sensors, along with GFS variables used as input, is listed in Table 1.

c. Surface precipitation estimation algorithm

As described above, a fully convolutional model with U-Net architecture (Fig. 1) is used to retrieve surface precipitation. In our study, adaptive moment estimation—the Adam optimizer—employs the first and second moments of the gradient to adapt the learning rate for each weight of the U-Net model. The high-quality GPM GV-MRMS precipitation products for May, June, July, August, and September of 2017–20 are used for calibration, validation, and testing of the model. The U-Net model with a mean-square-error (MSE) cost function is implemented using TensorFlow (version 2.5) and computes unified device architecture (CUDA) on multiple graphics processing units (GPUs). The details of the model architecture with its layer characteristics are presented in Table 2. It is important to acknowledge that training the U-Net model is conducted using GV-MRMS information.

d. Performance validation

We consider the widely used Pearson correlation coefficient (CORR), relative bias ratio (RBIAS), root-mean-square error (RMSE), critical success index (CSI), false alarm ratio (FAR), probability of detection (POD), volumetric CSI (VCSI), and volumetric FAR (VFAR) for evaluation of the U-Net surface-precipitation estimation algorithm performance. The validation statistics are defined in the appendix.

e. Model's input permutation importance

In an attempt to understand the importance of the inputs to the U-Net model, a permutation feature, importance, is defined as a decrease in the model's bias when a single input layer (i.e., predictor, an input feature) is replaced with a random noise. In other words, the importance of the input features is estimated based on the change in the retrieved bias when one or more input layers no longer contain meaningful information. In the first step, the benchmark score is defined as the performance of the model (i.e., calculated mean bias) with respect to the reference data during the test period. Then, the mean bias is calculated for the models when different combinations of predictors are replaced with random noises. Each of these altered biases is defined as the permuted score. The difference between the benchmark and permuted
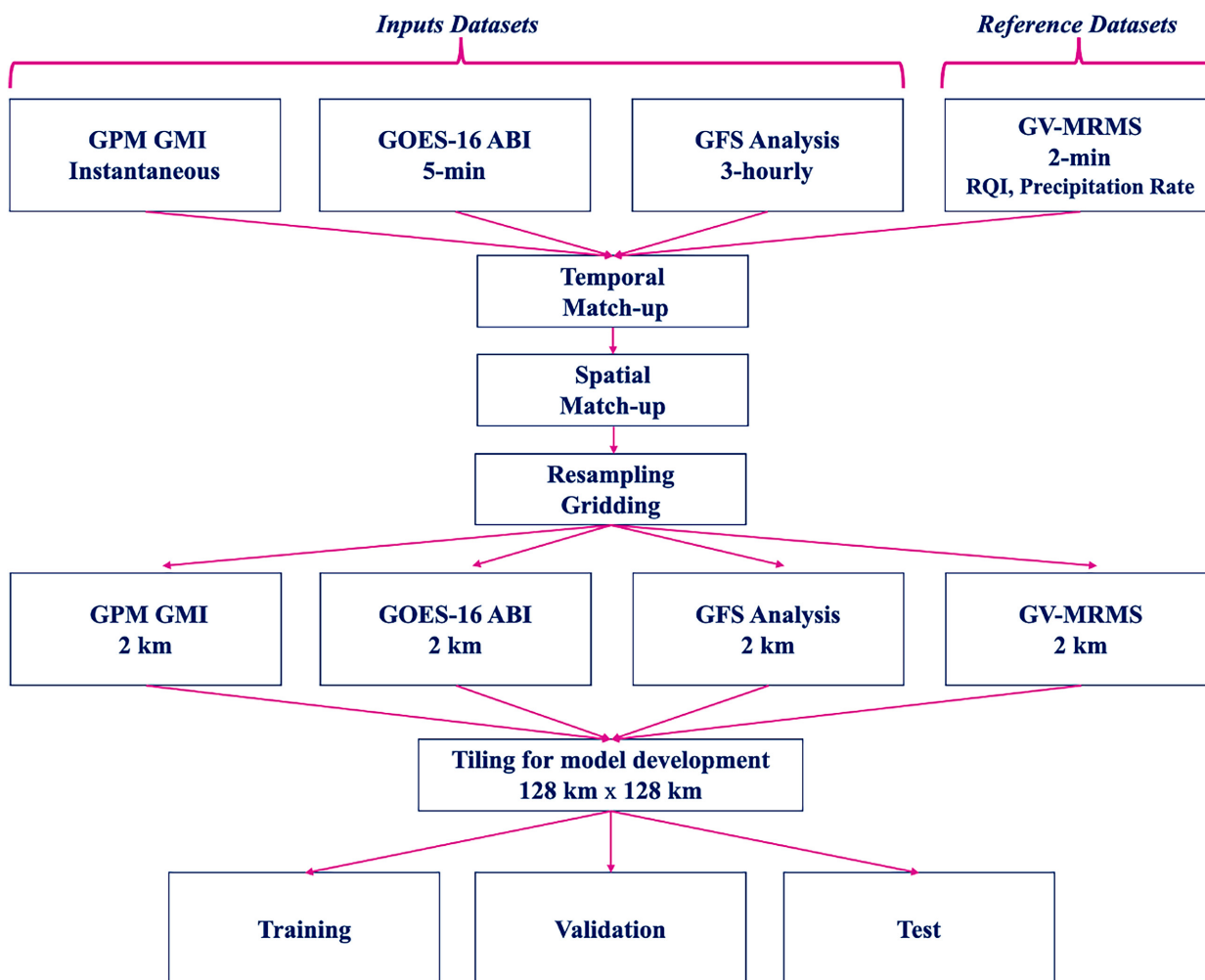
FIG. 3. An overview of data preprocessing.

scores for each of the altered inputs is the precipitation rate bias change, a metric of the input feature importance.

$$\text{precipitation rate bias change (\%)}$$
$$= \frac{\text{benchmark score (mm h}^{-1}) - \text{permuted score(mm h}^{-1})}{\text{benchmark score (mm h}^{-1})}$$
$$\times 100. \tag{3}$$

4. Result and discussion

The ABI multispectral remotely sensed information from 0.47 to 11.21 μm, GMI PMW Tbs from emission and scattering frequencies, and GFS T2m and PWAT are collocated and used to develop the U-Net algorithm. The quantification and categorical statistics of the model, benchmarked against MRMS surface precipitation estimates with the radar quality index greater than 80%, are reported in Table 3. The table includes the results corresponding to the test period (June–September 2020), considering the 0.1 mm h^{-1} precipitation rate threshold. To offer an insight on what can be considered a desirable performance level of an algorithm, Table 3 lists corresponding statistics of GPROF, GPROF-NN 3D (hereafter, GPROF-NN), and GPM DPR retrievals. With a correlation coefficient of 0.56, false detection rate of 18%, and POD score of 88%, the U-Net model is found to be successful in the tasks of precipitation detection and rate estimate. The RMSE index of 6.5 mm h^{-1} and CSI score of 0.81 suggest that model performs well in general precipitation detection. VCSI analysis indicates that 92% of the total volume of precipitation events is captured correctly, while 7% is found in the category of false alarms. The corresponding metrics of the globally calibrated GPROF retrieval confirm the high potential of the U-Net model. It should be noted that we utilize different precipitation retrievals during an independent test period (June–September of 2020) to show the discrepancies and challenges in current satellite algorithms, especially over complex surface types.

When compared against the MRMS product, the DPR captures 93% of the total volume of surface precipitation, while it is found to have a 20% false alarm score. Retrieved surface precipitation rates from DPR are 0.48 correlated to the MRMS product, showing relatively high RMSE with a

Table 1. List of satellite- and model-based features used as inputs to precipitation estimation algorithm.

	Source	Description	Original spatial resolution
1	GMI	10.65V GHz	19.4 km × 32.1 km
2	GMI	18.70H GHz	10.9 km × 18.1 km
3	GMI	23.80V GHz	9.7 km × 16 km
4	GMI	36.5V GHz	9.4 km × 15.6 km
5	GMI	36.5H GHz	9.4 km × 15.6 km
6	GMI	89 V GHz	4.4 km × 7.2 km
7	GMI	89H GHz	4.4 km × 7.2 km
8	GMI	166V GHz	4.1 km × 6.3 km
9	GMI	166H GHz	4.1 km × 6.3 km
10	GMI	183.31 ± 3V GHz	3.8 km × 5.8 km
11	G16-ABI	0.47 μm	1 km × 1 km
12	G16-ABI	0.64 μm	0.5 km × 0.5 km
13	G16-ABI	0.86 μm	1 km × 1 km
14	G16-ABI	1.37 μm	2 km × 2 km
15	G16-ABI	2.24 μm	2 km × 2 km
16	G16-ABI	3.90 μm	2 km × 2 km
17	G16-ABI	6.19 μm	2 km × 2 km
18	G16-ABI	6.93 μm	2 km × 2 km
19	G16-ABI	7.37 μm	2 km × 2 km
20	G16-ABI	8.44 μm	2 km × 2 km
21	G16-ABI	10.33 μm	2 km × 2 km
22	G16-ABI	11.21 μm	2 km × 2 km
23	Sun elevation angle	Degrees	2 km × 2 km
24	GFS PWAT	Total precipitable water (kg m^{-2})	0.25° × 0.25°
25	GFS T2m	2-m temperature (K)	0.25° × 0.25°

value of more than 7 mm h^{-1}. It should be noted that many factors limit the performance of DPR, such as significant surface clutter (Durden et al. 2020; Gou et al. 2018; Tang et al. 2017). The number of samples used to calculate verification metrics for DPR is approximately 1.8 million, while more than 41 million points are used in each of the PMW-based products statistics. The U-Net model is trained with respect to the MRMS precipitation product, targeting the warm season only. As such, if it is to be called successful, it must outperform retrievals intended for global all-season products (e.g., GPROF, DPR). The results presented here support the notion that an end-to-end DNN U-Net architecture can provide a high-quality precipitation rate product.

a. Qualitative assessment

As previously noted, one of the advantages of the U-Net model is the flexibility to process inputs of varying spatial extents. To achieve this, kernels are applied a different number

Table 2. U-Net architecture summary. The encoder operates on the input layer to extract robust features, the decoder constructs the output patterns and pixel values, and the bottleneck mediates between the encoder and decoder sections.

Layer #	1	2	3	4	5	6	7	8	9	10	11	12	13	14	15	16	17	18	19	20	21	22	23	24	25	26	27	28	29	30	31	32	33	34	35
Section	Encoder												Bottleneck						Decoder																
Layer	Input Layer	2D Convolution	Batch Normalization	Activation Function	2D Convolution	Batch Normalization	Activation Function	Maxpooling2D	2D Convolution	Batch Normalization	Activation Function	Maxpooling2D	2D Convolution	Batch Normalization	Activation Function	2D Convolution	Batch Normalization	Activation Function	Upsampling2D	Concatenate 11 and 19	2D Convolution	Batch Normalization	Activation Function	Upsampling2D	Concatenate 4 and 24	2D Convolution	Batch Normalization	Activation Function	2D Convolution	Batch Normalization	Activation Function	2D Convolution	Batch Normalization	Activation Function	2D Convolution
Output of Layer	64×64×25	64×64×16	64×64×16	64×64×16	64×64×8	64×64×8	64×64×8	32×32×8	32×32×16	32×32×16	32×32×16	16×16×16	16×16×32	16×16×32	16×16×32	16×16×32	16×16×32	16×16×32	32×32×32	32×32×48	32×32×16	32×32×16	32×32×16	64×64×32	64×64×32	64×64×32	64×64×32	64×64×16	64×64×16	64×64×16	64×64×8	64×64×8	64×64×8	64×64×8	64×64×1

TABLE 3. Performance of surface precipitation products from U-Net, GPROF, GPROF-NN, and DPR during June–September 2020. For each index, the best result is highlighted in bold.

Index\algorithm	Ideal value	U-Net	GPROF	GPROF-NN	DPR
CORR	1	**0.56**	0.38	0.37	0.48
RMSE (mm h^{-1})	0	6.46	5.70	**5.47**	7.33
RBIAS	1	**0.98**	0.96	0.88	0.88
POD	1	0.88	**0.89**	0.88	0.92
CSI	1	**0.81**	0.58	0.62	0.81
VCSI	1	**0.92**	0.83	0.79	0.93
FAR	0	**0.18**	0.41	0.37	0.20
VFAR	0	**0.07**	0.16	0.20	0.05

of times, depending on the input size over the spatial domain, allowing the output of the convolution operation to scale accordingly. In the present study, training is performed using about 110 000 elements of the size 64 pixels × 64 pixels × 25 layers (spatial domain: 128 km × 128 km, 25 input variables). Yet, the trained model supports various input/output dimensions. To show this practical characteristic of the U-Net algorithm, one case is visualized in Fig. 4. Figures 4a and 4b display 4 (of 25) selected input layers to the U-net model: PMW Tbs at 18.7H and 166H GHz frequencies, and ABI Tbs at 6.2 and 11.2 μm. These observations are associated with a GMI orbit (03666) overpass of the U.S. Midwest and parts of southeast of Canada at 0725 UTC 11 August. The spatial extent of each input is approximately 15° × 15°. The reference MRMR precipitation rates and the derived precipitation rates from the U-Net algorithm are shown in Fig. 4c. The presented case depicts the model's ability to capture fine-scale patterns of precipitation within and outside of the training domain during nighttime (0225 local time). Optimizing the performance of the model for the regions outside the training domain and investigating the nighttime ABI visible bands information content are beyond the scope of the study (no alteration of the nighttime ABI radiances is performed at any of the 16 bands).

Figure 5 displays a precipitation scene over the portions of Indiana, Illinois, and Kentucky, observed by ABI and GPM-*CO* sensors on 1 August 2020. The event is selected based on the availability of high-quality reference products and the presence of complex spatial patterns associated with the developing convective system. A set of selected U-Net input layers, shown in the top row, includes Tbs and radiances collected by ABI VIS/6.2-μm bands and GMI 18.7H/166 GHz channels. The VIS image is composed of three ABI channels, 0.47, 0.64, and 0.86 μm bands ("blue," "red," and "vegetation"); the three opaque ABI infrared bands (6.2–7.3 μm) are affected mainly by water vapor absorptions. These observations, intended to provide information on the atmospheric moisture content and temperature, are complemented by the upper-level water vapor band (~6.2 μm) sensitive to the top layers of the atmosphere. The same panel depicts Tbs from the low-frequency 18.7 GHz (emission) PMW band being significantly affected by land surface radiation (warm colors). In contrast,

the high-frequency 166 GHz GMI channel indicates ice-induced scattering within radiometric cold areas.

Qualitative comparisons of U-Net–, GPROF-NN–, and GPROF-retrieved surface precipitation rates to the MRMS and DPR reference products, as shown in Figs. 5b and 5c, confirm U-Net's ability to successfully fuse GEO and LEO (ABI and GMI) observations and take advantage of automatic spatial feature extraction using convolutional layers. Both NN-based algorithms, U-Net and GPROF-NN, adequately capture the spatial patterns of high- and low-intensity precipitation rates. Still, they slightly underestimate the precipitation rates over the northern and western parts of the event. Given the visual and general assessments, next we perform quantitative assessment of the U-Net algorithm performance.

b. Quantitative assessment

Figure 6 showcases the density scatterplots of U-Net, GPROF-NN, and GPROF surface precipitation rates (x axis) versus MRMS observations (y axis) for June–September 2020. Additionally, it displays the marginal distributions of each product as univariate histograms on the vertical and horizontal axes. Two precipitation types are defined using the MRMS product typology: 1) stratiform (warm stratiform, warm stratiform when radar data are above the melting layer, tropical stratiform mix, and cool stratiform), and 2) convective (hail, and tropical convective mix). Figure 6 shows the U-Net to MRMS surface precipitation rate correlation coefficients of 0.41 (stratiform) and 0.34 (convective) and multiplicative bias values of 0.97 (stratiform) and 0.64 (convective). This performance is well within the expected range of operational retrievals (as documented using GPROF-NN and GPROF examples). It is worth noting that the U-Net algorithm is not an exception when it comes to significantly underestimating low-intensity (<4 mm h^{-1}) and overestimating high-intensity (>10 mm h^{-1}) precipitation rates.

c. Assessment of surface precipitation estimation over different surface types

Figure 7 demonstrates the performance of U-Net, GPROF-NN, and GPROF-NN algorithms during the test period (June–September 2020) over four distinct surface types: ocean, land, orographic, and coastal. The surface types are adopted from the GPM GPROF, version 07, classification scheme (TELSEM), grouping the orographic and vegetated surface indices into single types named orographic and land, respectively. Given the investigation is focused on summertime, the classes related to snow- and ice-covered regions are excluded. Figure 7a indicates that algorithms tend to underestimate precipitation rates of less than 3 mm h^{-1} over the ocean surface type. The CORR value for U-Net is 0.58, with the total multiplicative bias of 0.86. While the higher correlation coefficient value is expected, the opposite RBIAS between U-Net and GPROF is likely to be a consequence of different ocean regions used in the training process (region-specific vs global) of the algorithms. It should be noted that radar-based GV-MRMS products used for training the U-Net have limited range over the ocean surface type—a "near-coast ocean" rather than "open ocean"—which may contribute to the difference in RBIAS between the U-Net and GPROF
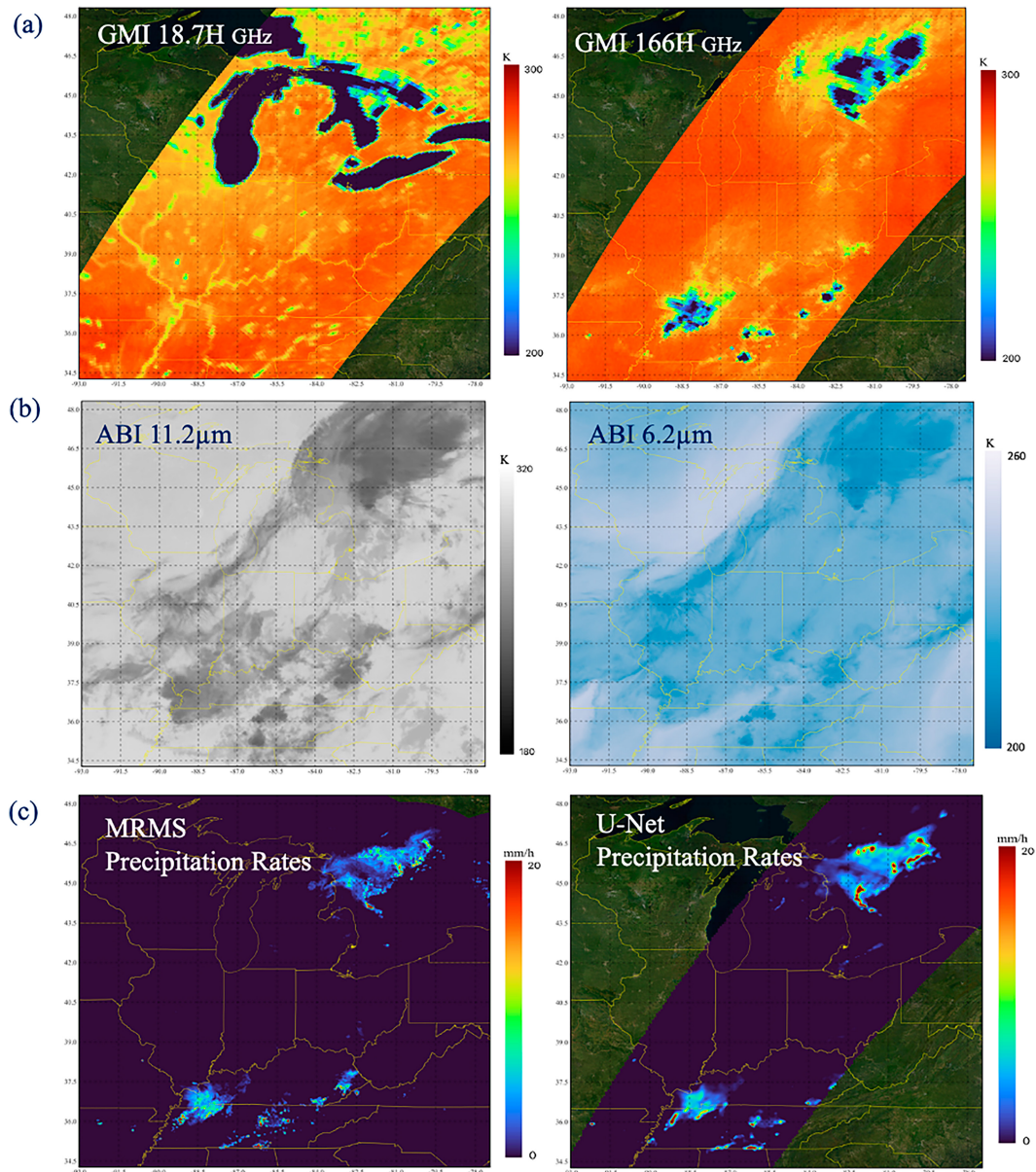
Fig. 4. Precipitation system observed at 0725 UTC 11 Aug 2020, over the U.S. Midwest. (a) GMI 18.7H and 166H GHz frequencies Tbs; (b) ABI 6.2 and 11.2 μm Tbs; (c) MRMS surface precipitation product and U-Net output.

ocean precipitation rates. The scatterplots and marginal distributions of precipitation rates show that U-Net performs well in detecting precipitation over land surfaces (Fig. 7b) with a correlation coefficient value of 0.57 and a multiplicative bias of 0.93.

Figures 7c and 7d demonstrate that the U-Net model is skillful in detecting the occurrence and amount of precipitation events over complex orographic and coastline regions. Significant discrepancies between the spread and general distribution of satellite retrievals and MRMS products are displayed across these complex regions. The CORR and RBIAS values for precipitation estimates derived from U-Net are 0.57 and 0.93, respectively. Over the coastlines, surface precipitation retrievals from U-Net are 0.59 correlated to the references. The

distribution of U-Net precipitation rates shows a similar spread compared to MRMS observations with the RBIAS value of 0.90. The retrieved surface precipitation distributions from GPROF and GPROF-NN models over all surface types show comparable marginal distribution. The presented results show the difficulties in retrieving surface precipitation systems by satellite algorithms over complex regions but suggest that addition of the ABI information (the U-Net retrieval) may be a key to finding a solution to this problem. Particularly, U-Net takes advantage of high-spatial-resolution GEO information to solve the challenge of PMW-only precipitation retrievals over mixed surface types where large PMW footprints tend to smooth out the variability in radiometric properties of the surface.

(a) Samples from Input Dataset
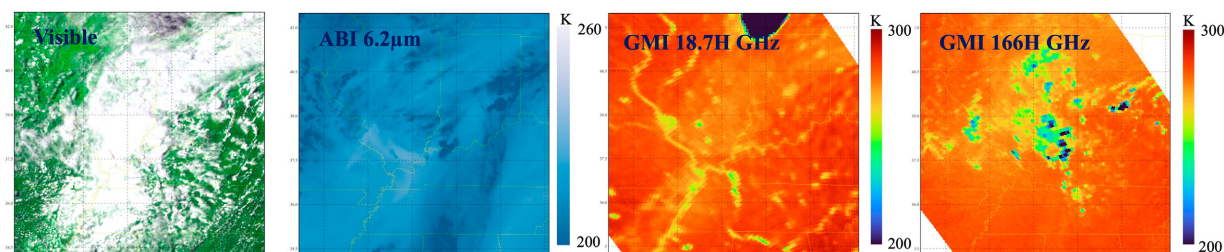
(b) MRMS and DPR Precipitation Rates
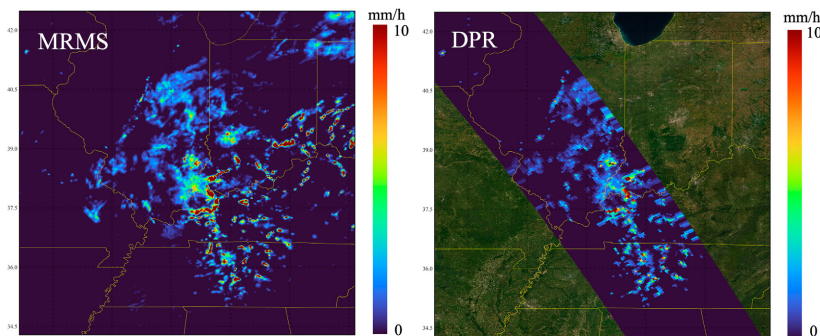
(c) Retrieved Precipitation Rates

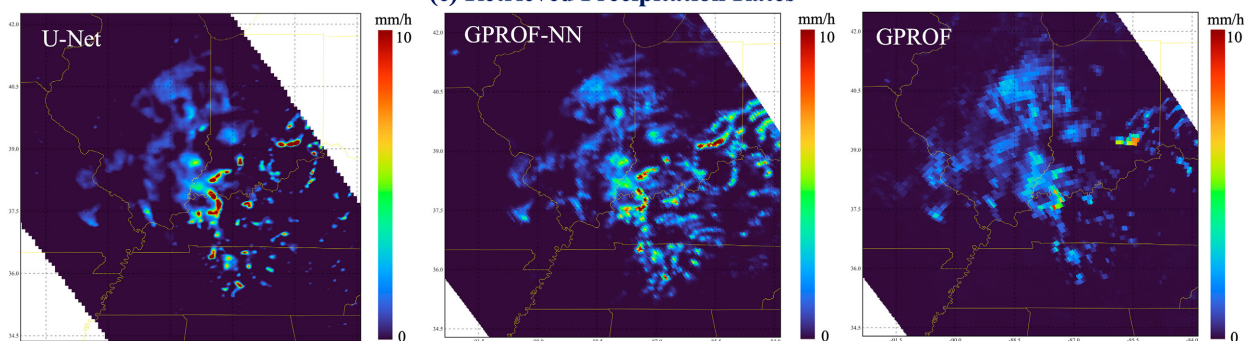
FIG. 5. Visualization of (a) the ABI visible bands' composition (0.47, 0.64, and 0.86 μm bands), ABI's 6.2 μm, GMI's 18.7H GHz, and GMI's 166H GHz; (b) MRMS surface precipitation rate (reference) and GPM DPR products; (c) retrieved surface precipitation rates from U-Net, GPROF-NN, and GPROF-NN at 1940 UTC 1 Aug 2020.

d. Input feature importance

Aiming to assess the impact of the input features on the U-Net model performance, similar to Gorooh et al. (2022a), a simple strategy is used to rank the model's input information content (predictors) with respect to their importance. As described in methodology, the trained model is used to retrieve the precipitation rate twice: the first time (baseline run) using all available inputs, and the second using random noise to replace one or more input layers. The change in the bias between the two outputs is then used to rank the importance of the input features (the higher the change, the stronger the impact of the input layer). In Fig. 8, the inputs (*y* axis) located at the top part of the graph have more impact on the model performance, while the inputs positioned toward the bottom part of the chart have less impact on the retrieved precipitation. The U-Net model favors PMW information in scattering

frequency bands, including 89V/H and 166V/H GHz. An obvious reason is that most retrieved precipitation is found over the land. Hence, the model relies on the scattering signal detected by high PMW frequencies responsive to the ice cloud content.

Next on the list are the ABI's 2.24 and 11.21 μm bands, followed by the PMW 18.7 GHz band. The 2.24 μm band is primarily sensitive to the cloud particle size and indicates the characteristics of cloud developments. The IR 11.21-μm band is similar to the legacy IR 10.7 μm band in cloud-overshooting-tops detections, although, in the 11.21 μm channel, there is more energy absorption by water vapor than in the 10.7 μm band. Over land, the 18.7 GHz band measurements are overwhelmed by the surface emissivity variability; thus, it provides relatively persistent information on the surface types to the model. Furthermore, this PMW band perfectly districts precipitation signatures over the radiometrically cold water and

(a) Stratiform Precipitation
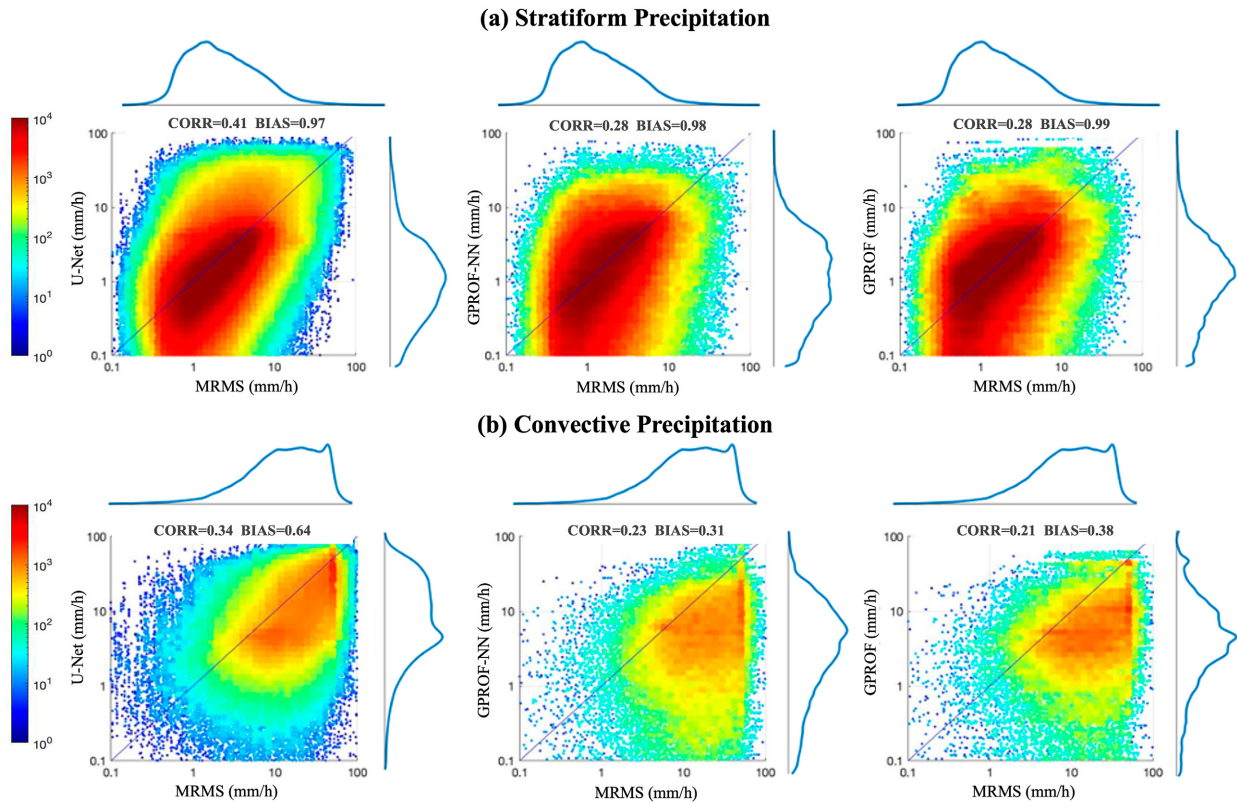

(b) Convective Precipitation

FIG. 6. Performance of U-Net, GPROF-NN, and GPROF surface precipitation retrievals with respect to MRMS. (a) Stratiform and (b) convective regime density plots for June–September 2020. The distributions of each product are shown next to the corresponding axes.

ocean backgrounds. These are followed by the VIS and NIR channels with approximate central wavelengths of 0.47–1.37 μm followed by water vapor bands (6.19–7.37 μm). Surface features are distinguishable in the daytime observations from blue (0.47 μm) and red (0.64 μm) VIS bands, while 1.37 μm as a reflective band is also able to detect low-level and cirrus cloud types during the day. The IR ABI water vapor bands provide information about the structure of the atmosphere in terms of temperature and moisture content at three levels. The 6.19 μm band, known as upper-level water vapor, provides information on potential areas for turbulence and upper-tropospheric winds, while 6.93 and 7.37 μm bands detect lower moisture content when the upper atmosphere is relatively dry. The ABI's 7.37 μm band also offers valuable information about convective cloud and convection initiations to the U-Net model. After these channels, the results indicate that the U-Net model sees GFS PWAT and T2m variables as the next most important input parameters. In the case of ">89H/V GHz," there is a drop in the performance of the model. However, it is found that using random noise to replace the input frequencies above 89H/V GHz channels does not alter the performance of the model severely (the >89H/V GHz scenario is located in the lower part of the plot in Fig. 8). Therefore, we believe that applying the U-Net algorithm to other GPM conical-scanning radiometers, with reduced information content, may not significantly limit the performance of the precipitation algorithm. Analyzing the U-Net algorithm's ability to perform on a non-GMI input [e.g., the case of Advanced Microwave Scanning

Radiometer-2 (AMSR2) PMW bands] is beyond the scope of this study.

5. Summary and conclusions

In this study, we investigate the applicability and potential of a U-Net architecture in the task of fusing multispectral, remotely sensed information from GEO and LEO sensors with GFS variables to retrieve summertime surface precipitation rate. An end-to-end deep learning technique is used to train a U-Net–like architecture and bypass the intermediate or feature-engineered stages typically seen in the process-oriented methods. The study's distinct goal was to test a U-net architecture suitability for a task of fusing complementing information content originating from various source to retrieve the summertime surface precipitation rate at high spatial resolution. In this effort, multiple satellite products providing observations in the VIS, NIR, and IR portions of the electromagnetic spectrum are integrated with PMW Tbs and auxiliary T2m and PWAT variables from the GFS model. The model is trained using ground-based radar observations collected during the period May–September 2017–19 over the eastern part of the CONUS, to deliver a 2-km-resolution output. The algorithm performance is assessed for ability to capture fine spatial patterns of surface precipitation events in different regimes (stratiform vs convective) and over different surface types during an
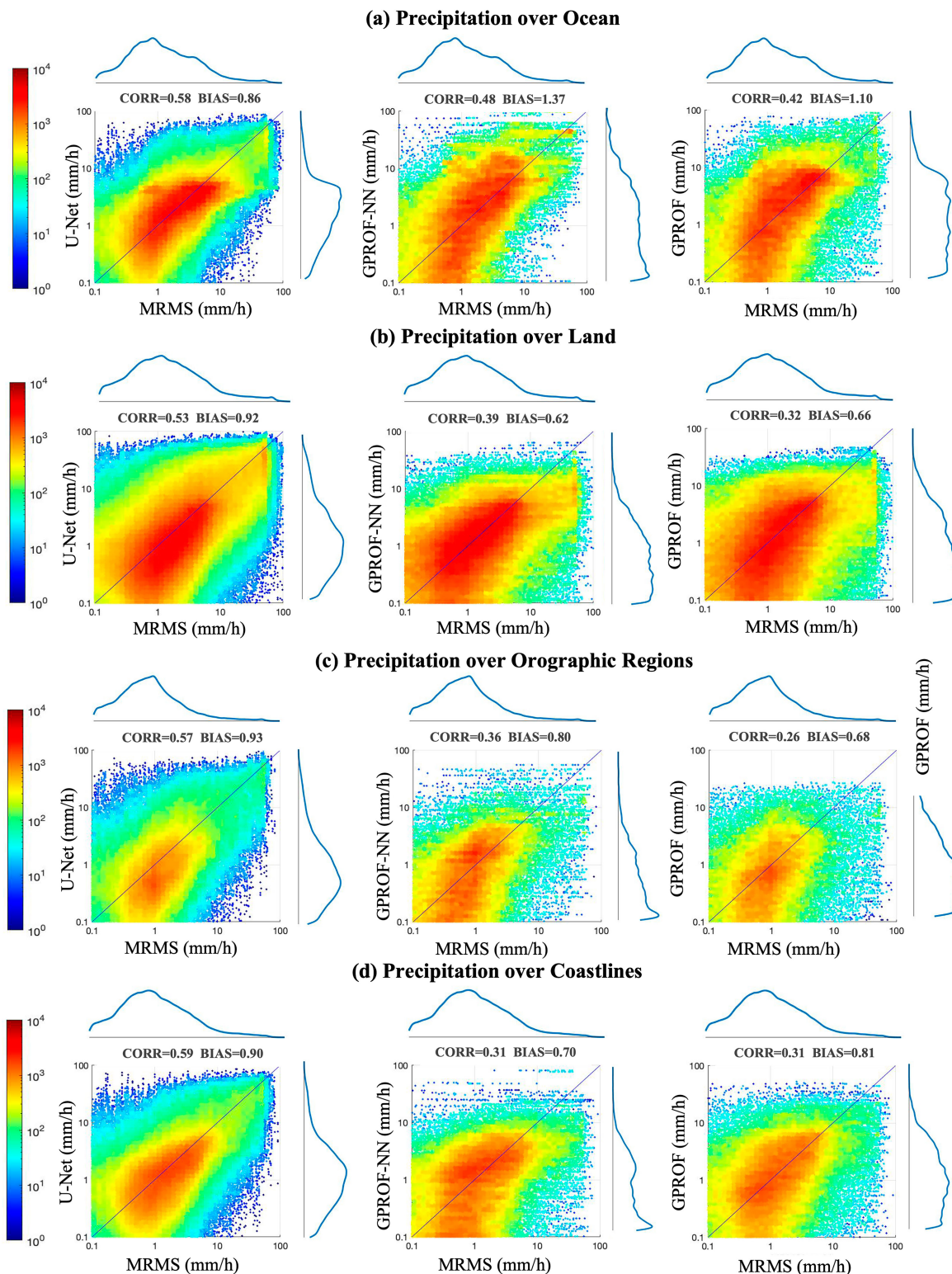
FIG. 7. Performance of surface precipitation retrievals for U-Net, GPROF-NN, and GPROF with respect to MRMS precipitation rates over (a) ocean, (b) land, (c) orographic, and (d) coastal surface types during June–September 2020. The distributions of each product are shown next to the corresponding axes.
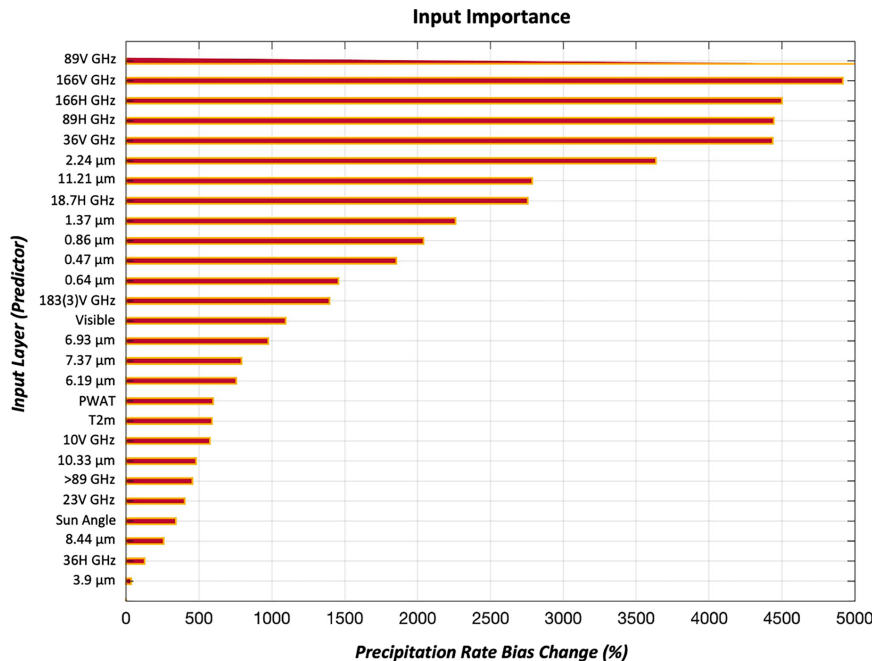
Input Importance

FIG. 8. U-Net's input-feature ranking. The precipitation rate bias variation (*x* axis) when a single input feature (*y* axis) of the retrieval is replaced by white noise.

independent test period (June–September 2020). The conclusions are summarized as follows:

- The U-Net model is skillful in terms of overall statistical indices and categorical and volumetric verification metrics. Our model reduces false alarms and improves general detection skills (e.g., CSI and VCSI) while showing relatively high total RMSE values.

- The performance of the U-Net algorithm highlights its ability to extract fine-scale spatial patterns of surface precipitation events at levels comparable to those seen in the state-of-the-art operational retrievals.

- Being a fully convolutional network that uses an automatic feature extraction approach, the model is flexible to process inputs of variable sizes and capable of fusing the swath-based PMW footprints with high spatiotemporal resolution and multispectral ABI images.

- The end-to-end DNN algorithm (a purely machine learning approach) can reach high accuracy in precipitation rate estimates over different regimes. The U-Net precipitation rate model is found to perform slightly better over stratiform than convective regimes.

- The U-Net algorithm performs well in capturing the occurrence and amount of precipitation events over complex orographic and coastal regions. The results demonstrate that fusing high-spatiotemporal-resolution observations from ABI and GFS auxiliary variables with LEO PMW observations enhances the spatial detection of surface precipitation during summertime over land, ocean, and coastal surface types under all precipitation regimes.

- Input-layer importance analysis confirms the expected origin of the information content, indicating that the model mainly relies on scattering frequencies from the LEO GMI radiometer, followed by 2.24 and 11.21 μm from GEO-based ABI. Afterward, ABI's VIS, NIR, and water vapor IR bands are listed as important inputs to our model.

The presented results reveal the potential U-Net architecture has in delivering high-spatial-resolution surface precipitation rate estimation by integrating sets of VIS, NIR, and IR information with PMW footprints along with PWAT and T2m auxiliary variables. The efficient end-to-end algorithm uses an automatic feature-extraction approach to extract and fuse LEO and GEO passively-sensed information to offer consistent results at low computational cost for high-spatial-resolution precipitation rate estimation. The presented framework is readily expandable to similar new generations of imagers, such as AHI, just as the considerations made here on the GMI can be applied to other current and future GPM conical-scanning PMW radiometers (e.g., AMSR2/3, MWI).

[Cooperative Institute for Satellite Earth System Studies (CISESS)] at the University of Maryland.

APPENDIX

Evalutation Metrics

The performance of precipitation retrievals is evaluated with Pearson CORR (perfect value = 1), RBIAS (ideal value = 1), and RMSE (ideal value = 0), as follows:

$$\text{CORR} = \frac{1}{n} \frac{\sum_{i=1}^{n}(P_i - \overline{P})(O_i - \overline{O})}{\sqrt{\sum_{i=1}^{n}(P_i - \overline{P})^2}\sqrt{\sum_{i=1}^{n}(O_i - \overline{O})^2}}$$

$$\text{RBIAS} = \frac{1}{n}\sum_{i=1}^{n}\frac{P_i}{O_i}$$

$$\text{RMSE} = \sqrt{\frac{1}{n}\sum_{i=1}^{n}(P_i - O_i)^2},$$

where P_i represents the ith satellite precipitation estimate, O_i refers to the corresponding reference observation, and n denotes the total number of samples. The perfect RBIAS value is 1. The POD (ideal value = 1), FAR (ideal value = 0), and CSI (ideal value = 1) are used for categorical assessments and are defined as follows:

$$\text{POD} = \frac{H}{H + M},$$

$$\text{FAR} = \frac{F}{F + H}$$

$$\text{CSI} = \frac{H}{H + F + M},$$

where H (hit) indicates that both the precipitation algorithm and reference observation detect the event, M (miss) identifies events observed by reference but missed by the precipitation estimation algorithm, and F (false alarm) indicates events not seen by reference yet detected by the precipitation estimation model. The VFAR and VCSI are used for volumetric categorical evaluation metrics. We consider 0.1 mm h^{-1} as the threshold t above which the volumetric indices are computed (Aghakouchak and Mehran 2013):

$$\text{VFAR} = \frac{\sum_{i=1}^{n}[P_i | (P_i > t \& O_i t)]}{\sum_{i=1}^{n}[P_i | (P_i > t \& O_i > t)] + \sum_{i=1}^{n}[P_i | (P_i > t \& O_i t)]},$$

$$\text{VCSI} = \frac{\sum_{i=1}^{n}[P_i | (P_i > t \& O_i > t)]}{\sum_{i=1}^{n}[P_i | (P_i > t \& O_i > t)] + \sum_{i=1}^{n}[P_i | (O_i t \& O_i > t)] + \sum_{i=1}^{n}[P_i | (P_i < t \& O_i t)]}.$$

REFERENCES

Adler, R. F., A. J. Negri, P. R. Keehn, and I. M. Hakkarinen, 1993: Estimation of monthly rainfall over Japan and surrounding waters from a combination of low-orbit microwave and geosynchronous IR data. *J. Appl. Meteor.*, **32**, 335–356, https://doi.org/10.1175/1520-0450(1993)032<0335:EOMROJ>2.0.CO;2.

Aghakouchak, A., and A. Mehran, 2013: Extended contingency table: Performance metrics for satellite observations and climate model simulations. *Water Resour. Res.*, **49**, 7144–7149, https://doi.org/10.1002/wrcr.20498.

Aires, F., C. Prigent, F. Bernardo, C. Jiménez, R. Saunders, and P. Brunel, 2011: A Tool to Estimate Land-Surface Emissivities at Microwave Frequencies (TELSEM) for use in numerical weather prediction. *Quart. J. Roy. Meteor. Soc.*, **137**, 690–699, https://doi.org/10.1002/qj.803.

Akbari Asanjan, A., T. Yang, K. Hsu, S. Sorooshian, J. Lin, and Q. Peng, 2018: Short-term precipitation forecast based on the PERSIANN system and LSTM recurrent neural networks. *J. Geophys. Res. Atmos.*, **123**, 12 543–12 563, https://doi.org/10.1029/2018JD028375.

Aonashi, K., and Coauthors, 2009: GSMaP passive microwave precipitation retrieval algorithm: Algorithm description and validation. *J. Meteor. Soc. Japan*, **87A**, 119–136, https://doi.org/10.2151/jmsj.87A.119.

Arkin, P. A., and P. E. Ardanuy, 1989: Estimating climatic-scale precipitation from space: A review. *J. Climate*, **2**, 1229–1238, https://doi.org/10.1175/1520-0442(1989)002<1229:ECSPFS>2.0.CO;2.

Beck, H. E., and Coauthors, 2019: Daily evaluation of 26 precipitation datasets using stage-IV gauge-radar data for the CONUS. *Hydrol. Earth Syst. Sci.*, **23**, 207–224, https://doi.org/10.5194/hess-23-207-2019.

Behrangi, A., K.-L. Hsu, B. Imam, S. Sorooshian, and R. J. Kuligowski, 2009: Evaluating the utility of multispectral information in delineating the areal extent of precipitation. *J. Hydrometeor.*, **10**, 684–700, https://doi.org/10.1175/2009JHM1077.1.

Draper, D. W., D. A. Newell, F. J. Wentz, S. Krimchansky, and G. M. Skofronick-Jackson, 2015: The Global Precipitation Measurement (GPM) microwave imager (GMI): Instrument overview and early on-orbit performance. *IEEE J. Sel. Top. Appl. Earth Obs. Remote Sens.*, **8**, 3452–3462, https://doi.org/10.1109/JSTARS.2015.2403303.

Durden, S. L., S. Tanelli, and O. O. Sy, 2020: Comparison of GPM DPR and airborne radar observations in OLYMPEX. *IEEE Geosci. Remote Sens. Lett.*, **17**, 1707–1711, https://doi.org/10.1109/LGRS.2019.2952287.

Ehsani, M. R., A. Zarei, H. V. Gupta, K. Barnard, and A. Behrangi, 2021: Nowcasting-nets: Deep neural network structures for precipitation nowcasting using IMERG. arXiv, 2108.06868v1, https://doi.org/10.48550/arXiv.2108.06868.

Ferraro, R. R., 1997: Special sensor microwave imager derived global rainfall estimates for climatological applications. *J. Geophys. Res.*, **102**, 16715–16735, https://doi.org/10.1029/97JD01210.

Foufoula-Georgiou, E., and Coauthors, 2020: Advancing precipitation estimation, prediction, and impact studies. *Bull. Amer. Meteor. Soc.*, **101**, E1584–E1592, https://doi.org/10.1175/BAMS-D-20-0014.1.

Goodfellow, I., Y. Bengio, and A. Courville, 2016: *Deep Learning.* MIT Press, 800 pp.

Gorooh, V. A., A. A. Asanjan, P. Nguyen, K. Hsu, and S. Sorooshian, 2022a: Deep Neural Network High Spatiotemporal Resolution Precipitation Estimation (Deep-STEP) using passive microwave and infrared data. *J. Hydrometeor.*, **23**, 597–617, https://doi.org/10.1175/JHM-D-21-0194.1.

——, E. J. Shearer, P. Nguyen, K. Hsu, S. Sorooshian, F. Cannon, and M. Ralph, 2022b: Performance of new near-real-time PERSIANN product (PDIR-now) for atmospheric river events over the Russian River basin, California. *J. Hydrometeor.*, **23**, 1899–1911, https://doi.org/10.1175/JHM-D-22-0066.1.

Gou, Y., Y. Ma, H. Chen, and Y. Wen, 2018: Radar-derived quantitative precipitation estimation in complex terrain over the eastern Tibetan Plateau. *Atmos. Res.*, **203**, 286–297, https://doi.org/10.1016/j.atmosres.2017.12.017.

Hayatbini, N., and Coauthors, 2019: Conditional generative adversarial networks (cGANs) for near real-time precipitation estimation from multispectral *GOES-16* satellite imageries—PERSIANN-cGAN. *Remote Sens.*, **11**, 2193, https://doi.org/10.3390/rs11192193.

Hirose, H., S. Shige, M. K. Yamamoto, and A. Higuchi, 2019: High temporal rainfall estimations from *Himawari-8* multiband observations using the random-forest machine-learning method. *J. Meteor. Soc. Japan*, **97**, 689–710, https://doi.org/10.2151/jmsj.2019-040.

Hong, Y., K.-L. Hsu, S. Sorooshian, and X. Gao, 2004: Precipitation estimation from remotely sensed imagery using an artificial neural network cloud classification system. *J. Appl. Meteor.*, **43**, 1834–1853, https://doi.org/10.1175/JAM2173.1.

Hou, A. Y., and Coauthors, 2014: The Global Precipitation Measurement mission. *Bull. Amer. Meteor. Soc.*, **95**, 701–722, https://doi.org/10.1175/BAMS-D-13-00164.1.

Hsu, K.-L., X. Gao, S. Sorooshian, and H. V. Gupta, 1997: Precipitation estimation from remotely sensed information using artificial neural networks. *J. Appl. Meteor.*, **36**, 1176–1190, https://doi.org/10.1175/1520-0450(1997)036<1176:PEFRSI>2.0.CO;2.

Joyce, R. J., J. E. Janowiak, P. A. Arkin, and P. Xie, 2004: CMORPH: A method that produces global precipitation estimates from passive microwave and infrared data at high spatial and temporal resolution. *J. Hydrometeor.*, **5**, 487–503, https://doi.org/10.1175/1525-7541(2004)005%3C0487:CAMTPG%3E2.0.CO;2.

Kalogirou, S. A., 2022: Solar thermal systems: Components and applications—Introduction. *Comprehensive Renewable Energy*, T. Letcher, Ed., Elsevier, 1–25.

Kidd, C., and V. Levizzani, 2011: Status of satellite precipitation retrievals. *Hydrol. Earth Syst. Sci.*, **15**, 1109–1116, https://doi.org/10.5194/hess-15-1109-2011.

Kirstetter, P. E., and Coauthors, 2012: Toward a framework for systematic error modeling of spaceborne precipitation radar with NOAA/NSSL ground radar–based national mosaic QPE. *J. Hydrometeor.*, **13**, 1285–1300, https://doi.org/10.1175/JHM-D-11-0139.1.

Kuligowski, R. J., Y. Li, Y. Hao, and Y. Zhang, 2016: Improvements to the GOES-R rainfall rate algorithm. *J. Hydrometeor.*, **17**, 1693–1704, https://doi.org/10.1175/JHM-D-15-0186.1.

Kummerow, C. D., D. L. Randel, M. Kulie, N.-Y. Wang, R. Ferraro, S. Joseph Munchak, and V. Petkovic, 2015: The evolution of the Goddard profiling algorithm to a fully parametric scheme. *J. Atmos. Oceanic Technol.*, **32**, 2265–2280, https://doi.org/10.1175/JTECH-D-15-0039.1.

Li, Z., Y. Wen, M. Schreier, A. Behrangi, Y. Hong, and B. Lambrigtsen, 2021: Advancing satellite precipitation retrievals with data driven approaches: Is black box model explainable? *Earth Space Sci.*, **8**, e2020EA001423, https://doi.org/10.1029/2020EA001423.

Ma, X., A. Huete, N. N. Tran, J. Bi, S. Gao, and Y. Zeng, 2020: Sun-angle effects on remote-sensing phenology observed and modelled using Himawari-8. *Remote Sens.*, **12**, 1339, https://doi.org/10.3390/rs12081339.

Mallakpour, I., M. Sadeghi, H. Mosaffa, A. Akbari Asanjan, M. Sadegh, P. Nguyen, S. Sorooshian, and A. AghaKouchak, 2022: Discrepancies in changes in precipitation characteristics over the contiguous United States based on six daily gridded precipitation datasets. *Wea. Climate Extremes*, **36**, 100433, https://doi.org/10.1016/j.wace.2022.100433.

Meyer, H., M. Kühnlein, C. Reudenbach, and T. Nauss, 2017: Revealing the potential of spectral and textural predictor variables in a neural network-based rainfall retrieval technique. *Remote Sens. Lett.*, **8**, 647–656, https://doi.org/10.1080/2150704X.2017.1312026.

Min, M., and Coauthors, 2019: Estimating summertime precipitation from Himawari-8 and global forecast system based on machine learning. *IEEE Trans. Geosci. Remote Sens.*, **57**, 2557–2570, https://doi.org/10.1109/TGRS.2018.2874950.

Nguyen, P., E. J. Shearer, M. Ombadi, V. A. Gorooh, K. Hsu, S. Sorooshian, W. S. Logan, and M. Ralph, 2020a: PERSIANN Dynamic Infrared–Rain Rate model (PDIR) for high-resolution, real-time satellite precipitation estimation. *Bull. Amer. Meteor. Soc.*, **101**, E286–E302, https://doi.org/10.1175/BAMS-D-19-0118.1.

——, and Coauthors, 2020b: PERSIANN Dynamic Infrared–Rain Rate (PDIR-Now): A near-real-time, quasi-global satellite precipitation dataset. *J. Hydrometeor.*, **21**, 2893–2906, https://doi.org/10.1175/JHM-D-20-0177.1.

Ouallouche, F., M. Lazri, and S. Ameur, 2018: Improvement of rainfall estimation from MSG data using random forests classification and regression. *Atmos. Res.*, **211**, 62–72, https://doi.org/10.1016/j.atmosres.2018.05.001.

Pfreundschuh, S., P. J. Brown, C. D. Kummerow, P. Eriksson, and T. Norrestad, 2022: GPROF-NN: A neural-network-based implementation of the Goddard profiling algorithm. *Atmos. Meas. Tech.*, **15**, 5033–5060, https://doi.org/10.5194/amt-15-5033-2022.

Prigent, C., F. Aires, and W. B. Rossow, 2003: Retrieval of surface and atmospheric geophysical variables over snow-covered land from combined microwave and infrared satellite observations. *J. Appl. Meteor.*, **42**, 368–380, https://doi.org/10.1175/1520-0450(2003)042<0368:ROSAAG>2.0.CO;2.

Ronneberger, O., P. Fischer, and T. Brox, 2015: U-Net: Convolutional networks for biomedical image segmentation. *Medical Image Computing and Computer-Assisted Intervention–MICCAI 2015*, N. Navab et al., Eds., Lecture Notes in Computer Science, Vol. 9351, Springer, 234–241.

Rukundo, O., and H. Cao, 2012: Nearest neighbor value interpolation. *Int. J. Adv. Comput. Sci. Appl.*, **3**, 25–30, https://doi.org/10.14569/IJACSA.2012.030405.

Sadeghi, M., P. Nguyen, K. Hsu, and S. Sorooshian, 2020: Improving near real-time precipitation estimation using a U-Net convolutional neural network and geographical information. *Environ. Modell. Software*, **134**, 104856, https://doi.org/10.1016/j.envsoft.2020.104856.

Saemian, P., and Coauthors, 2021: Comprehensive evaluation of precipitation datasets over Iran. *J. Hydrol.*, **603**, 127054, https://doi.org/10.1016/j.jhydrol.2021.127054.

Sanò, P., G. Panegrossi, D. Casella, A. C. Marra, F. di Paola, and S. Dietrich, 2016: The new Passive Microwave Neural Network Precipitation Retrieval (PNPR) algorithm for the cross-track scanning ATMS radiometer: Description and verification study over Europe and Africa using GPM and TRMM spaceborne radars. *Atmos. Meas. Tech.*, **9**, 5441–5460, https://doi.org/10.5194/amt-9-5441-2016.

Schmit, T. J., P. Griffith, M. M. Gunshor, J. M. Daniels, S. J. Goodman, and W. J. Lebair, 2017: A closer look at the ABI on the GOES-R series. *Bull. Amer. Meteor. Soc.*, **98**, 681–698, https://doi.org/10.1175/BAMS-D-15-00230.1.

Scofield, R. A., and R. J. Kuligowski, 2003: Status and outlook of operational satellite precipitation algorithms for extreme-precipitation events. *Wea. Forecasting*, **18**, 1037–1051, https://doi.org/10.1175/1520-0434(2003)018<1037:SAOOOS>2.0.CO;2.

Skofronick-Jackson, G., and Coauthors, 2017: The Global Precipitation Measurement (GPM) mission for science and society.

Bull. Amer. Meteor. Soc., **98**, 1679–1695, https://doi.org/10.1175/BAMS-D-15-00306.1.

Sorooshian, S., K.-L. Hsu, X. Gao, H. V. Gupta, B. Imam, and D. Braithwaite, 2000: Evaluation of PERSIANN system satellite-based estimates of tropical rainfall. *Bull. Amer. Meteor. Soc.*, **81**, 2035–2046, https://doi.org/10.1175/1520-0477(2000)081<2035:EOPSSE>2.3.CO;2.

Tang, G., Y. Wen, J. Gao, D. Long, Y. Ma, W. Wan, and Y. Hong, 2017: Similarities and differences between three coexisting spaceborne radars in global rainfall and snowfall estimation. *Water Resour. Res.*, **53**, 3835–3853, https://doi.org/10.1002/2016WR019961.

Upadhyaya, S. A., P.-E. Kirstetter, R. J. Kuligowski, and M. Searls, 2022a: Exploring the temporal information from GEO satellites for estimating precipitation with convolutional neural networks. *IEEE Geosci. Remote Sens. Lett.*, **19**, 1–5, https://doi.org/10.1109/LGRS.2022.3189535.

——, ——, ——, and ——, 2022b: Towards improved precipitation estimation with the GOES-16 advanced baseline imager: Algorithm and evaluation. *Quart. J. Roy. Meteor. Soc.*, **148**, 3406–3427, https://doi.org/10.1002/qj.4368.

Utsumi, N., F. J. Turk, Z. S. Haddad, P.-E. Kirstetter, and H. Kim, 2021: Evaluation of precipitation vertical profiles estimated by GPM-era satellite-based passive microwave retrievals. *J. Hydrometeor.*, **22**, 95–112, https://doi.org/10.1175/JHM-D-20-0160.1.

Wang, W., S. Li, H. Hashimoto, H. Takenaka, A. Higuchi, S. Kalluri, and R. Nemani, 2020: An introduction to the Geostationary-NASA Earth Exchange (GeoNEX) Products: 1. Top-of-atmosphere reflectance and brightness temperature. *Remote Sens.*, **12**, 1267, https://doi.org/10.3390/rs12081267.

You, Y., V. Petkovic, J. Tan, R. Kroodsma, W. Berg, C. Kidd, and C. Peters-Lidard, 2020: Evaluation of V05 precipitation estimates from GPM constellation radiometers using KuPR as the reference. *J. Hydrometeor.*, **21**, 705–728, https://doi.org/10.1175/JHM-D-19-0144.1.

Zhang, J., and Coauthors, 2016: Multi-Radar Multi-Sensor (MRMS) quantitative precipitation estimation: Initial operating capabilities. *Bull. Amer. Meteor. Soc.*, **97**, 621–638, https://doi.org/10.1175/BAMS-D-14-00174.1.